Nils Klasen *et al.*, http://dx.doi.org/10.2139/ssrn.3152478, workshop homepage:
http://www.metallizationworkshop.info.

7th Workshop on Metallization and Interconnection for Crystalline Silicon Solar Cells, 2017

Shingled Cell Interconnection: A new Generation of Bifacial PV-Modules

Nils Klasen[a,b,1], Andrew Mondon[a], Achim Kraft[a], Ulrich Eitner[a]

[a]*Fraunhofer Institute for Solar Energy Systems ISE, Heidenhofstraße 2, 79110 Freiburg, Germany*
[b]*Institute for Applied Materials (IAM), Hermann-von-Helmholtz-Platz 1, 76334 Eggenstein-Leopoldshafen, Germany*

Abstract

The idea to interconnect solar cells in a shingled manner like roof tiles dates back to the 1960's [1]. However, the standard interconnection technology in the PV industry nowadays is still the front to back series interconnection using solder coated copper ribbons. Shingle interconnection offers very high packing densities of solar cells and increases the module's active area by eliminating busbars from the illuminated area. Direct interconnection of stripe-like solar cells by electrical conductive adhesives (ECA) replaces the front-to-back ribbon interconnection and therefore eliminates the interconnectors' ohmic losses. Stripe-like solar cells additionally reduce the overall ohmic losses of the solar cell string by lower cell currents.

In this work we provide an overview of the scientific state of the art and a summary of the most important features for shingled cell interconnection. We compare two calculation approaches for the joint deformation due to thermal expansion of the module materials and identify the most relevant parameters. The results show that the thickness of the joint material typically ranging from $\sim 20 - 100$ µm is crucial to reduce the shear deformation and therefore enabling sufficient long-term stability. Other geometrical parameters like the overlap width or number of solar cells per string only show a small effect on shear strain for cell widths > 20 mm. First experimental prototypes of shingled mini-modules of bifacial pSPEER solar cells using low temperature soldering (Sn42Bi58) show a total power loss of < 5 % after accelerated TC200 testing.

Peer-review under responsibility of the organizing committee of the 7th Workshop on Metallization and Interconnection for Crystalline Silicon Solar Cells

Keywords: Shingling; Bifacial Solar Modules; pSPEER

1. Introduction

Efficiency levels beyond 22 % are reached in industry on industrial PERC solar cell structures [2]. Increasing technology-level and economic competitiveness have led to a constant increase in market share of PERC-based PV-modules. We are focusing our research on novel module concepts and interconnection technologies in order to further increase the module efficiency based on PERC solar cell architectures. Recently, one type of cell interconnection catches great attention in the PV community after being developed already in 1960 [1]: cell shingling. In contrast to state of the art interconnection technologies, shingling does not require any extra cell interconnecting component such as ribbons or wires. Adjacent solar cells are overlapped and connected using either electrically conductive adhesives (ECA) or solder. This results in additional requirements for the joint between shingled solar cells. In general, external mechanical loads and temperature changes cause relative movement of the solar cells in the laminate [3]. Since the rigid solar cells are joined directly to each other, there is only one

* Corresponding author.
E-mail address: nils.klasen@ise.fraunhofer.de

component able to compensate the relative displacement: the joint material. In a first part of this study we compare two simplified theoretical approaches to calculate the shear deformation of the joint. Parameter studies of the geometrical variables examine their influence on shear strain when changing the temperature by 125 K which corresponds to the temperature interval of an IEC 61215 thermocycle test. In the second part we present first prototyping results of module integration of bifacial solar cells developed at Fraunhofer ISE especially for shingled modules.

1.1 Shingled cell interconnection

In a conventional PV module solar cells are interconnected in series by soldering copper ribbons to the front busbar of one cell as well as to the rear side of the neighboring cell (Fig. 1a). When it comes to shingling the series interconnection of the cells is established by a direct contact of the cell front side to the rear side of the next cell resulting in a cell overlap as depicted in Fig. 1b.

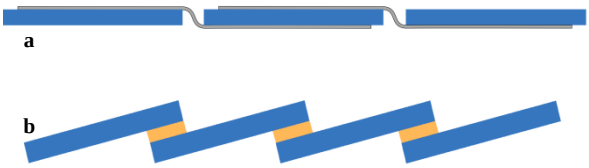

Fig. 1. Schematic drawing of conventional copper-ribbon interconnection (a) and shingle interconnection (b) for silicon solar cells.

When aiming for solar cell stripes of one sixth of a 6" solar cell the finger metallization layouts are similar to standard 3BB cells, as current transportation distances in the fingers are equal. The busbars of shingled cells are situated in the overlap. Focusing on the cell properties only, an optimal width has been calculated to be $15 - 26$ mm [4, 5], which is in good accordance to the size of one sixth of standard cells as previously stated . Current transportation from one cell to the next is established by a conductive joint material either solder or, more favorable, ECAs. ECAs tend to be mechanically more compliant than solders which we regard to be a key factor for module reliability especially when it comes to thermomechanical stresses. We discuss this aspect in chapter 1.3 of this work.

Compared to conventional module processing shingling requires the following aspects to be considered:

- Approx. $2 - 8$ % higher silicon usage due to overlapping regions.
- Additional process step due to cell separation and edge passivation. Potential risk for cell breakage.
- String assembly and string handling are more complex. Per module there are six times more cells which need to be interconnected affecting the process throughput.

On the other hand, shingling offers conceptual advantages aiming for very high module efficiencies:

- No busbar / ribbon shading of the solar cells since busbars are located in the overlap, which is covered by the next solar cells active area. This leads to an increase of the module's overall photosensitive area.
- No ohmic losses in copper ribbons for cell interconnection, since this element is eliminated completely.
- Increased active module area covered by solar cells due to elimination of cell spacing (in string direction).
- Decreased string currents due to smaller cells cause a reduction of ohmic losses, since solar cells for shingling are usually $1/6^{th}$ of conventional 6" cells.

These advantages result in an estimated efficiency gain of ~ 2 % absolute comparing a module using the shingle approach to a module using ribbon based interconnection [6]. Furthermore, the use of ECAs instead of today's state of the art lead-based solders drastically decreases the share of lead in the module. In conventional modules reflecting ribbons and visible cell spacings create non-regular patterns in PV modules resulting in poor aesthetics. Shingled modules feature a very homogeneous impression and are therefore well suited as uniform elements for building or facade integration.

1.2 The History of shingled interconnection for solar cells

Only six years after the first silicon solar cell with a p-n-junction had been published by Chapin, Fuller and Pearson [7] the shingled cell interconnection was first published by Dickson et al [1]. Since then this technique was mainly found in early space applications [8] to provide electric energy for satellites e.g. within the TIROS and the Explorer program [9]. In the 1970s Mobil Tyco worked on polycrystalline silicon modules employing shingle interconnection with the aim to demonstrate efficiencies > 8 % at costs of 0.5 $/W for a PV-array [10]. Back then the technique did not manage to compete with established silicon PV-technologies. With the development of ECAs in the 1980s shingling became an interesting technique to join thin-film amorphous silicon solar cells [11], since ECA curing temperatures offer low temperature processing as required for amorphous silicon. But still shingling remained to be a niche-technology for very high efficient applications, like the winning car of the 1996 World Solar Challenge and several other cars competing in the race through Australia [12, 13]. In 1990 Schmidt and Rasch demonstrated highly efficient shingled solar modules [14] with packing densities over 96 % based on shingling. They were able to show that, compared to conventional interconnection methods, their modules reach a very high cell-to-module (CTM) ratio losing only 0.4 % absolute in efficiency for both poly- and monocrystalline silicon solar modules. This lead to a new module efficiency record (23.1 %) in 1997 [15]. Other attempts in the late 1990s and early 2000s used shingling for mobile telephone integration [16] and thermophotovoltaics (TPV) [17, 18], bridging also the gap to III-V thin-film semiconductors. Other thin-film photo-absorbers like CIGS [19–22] and GaAs followed using shingle interconnection [23].

In summary, shingling has been found in highly specialized niche applications since its development in 1960. Nevertheless industry recently caught great interest in this technology and introduced commercial shingled modules to the market. Several patents exist on this technology [24–27]. They all have the basic principle of overlapping solar cells in common but differ in detailed aspects of interconnection. Some describe a special way of curing the joint material [28], others combine a multiwire approach with shingling [29] or realize a combined serial and parallel interconnection of each solar cell [30].

2. Theoretical investigation of the shingle joint

2.1. Thermomechanical considerations

Thermomechanical stress plays a major role in respect to module reliability, since materials with different CTEs are bonded together and subjected to temperature changes of up to 125 K during IEC 61215 conform thermocycling. Table 1 shows typical coefficients of thermal expansion of the different materials in a PV module. In the case of shingle interconnection the relative movement of the solar cells due to extension and contraction causes a shear deformation of the joint material, which may result in interconnection failure. Thermal expansion is considered to cause only lateral movement of the cells, because tilting angles towards the glass pane of 25 mm wide shingle cells with a joint thickness of up to 100 µm are well below 1 °. Hence cells in the module stack are also considered plane-parallel to the rest of the module stack layers. The expansion of the module is mainly forced by the glass pane, since it is by far the thickest component in the material stack [3].

Table 1. Coefficients of Thermal Expansion of materials used for the calculations.

Material	CTE (10^{-6} 1/K)
Float Glass	8.5
EVA	250.0
Silicon	2.5
ECA	50.0
Sn42Bi58	15.0
Backsheet	50.0

Two approaches to estimate the deformation of the shingle joint are discussed. There are three geometrical parameters influencing the shear strain of the shingle joint in both cases. A fourth, the number of cells, however, alters shear strain only in Eq. 1. The following parameters are varied for the parameter studies.

- Cell width l_0 and number n
- Overlap width x_O
- Joint thickness t

If not subject to variations the following the parameters are set to a default value. These are: $\Delta T = 125$ K, $x_O = 2$ mm, $l_0 = 23$ mm, $n = 30$ and $t = 50$ µm.

2.2 Model A: thermomechanical induced strain considering fixed bearings at start and final points of the cell string

An approximation for calculating the relative shift of the shingles (Eq. 1) provided by Beaucarne [31] is used to scan different joint design criteria for their relevance in causing thermomechanical stresses (Fig. 2). The model assumes the reference length of the glass L_0 to be equal to the sum of all interconnected cells. Strain is then caused by extension and compression of the glass and equally distributed over the joints of the string. The model assumes the string to be fixed to the glass pane on the edge of the first cell as well as the edge of the last cell. Eq. 1 is used to calculate the strain of a single shingle joint. A more detailed description of the derivation of Eq. 1 is given in [31].

$$\gamma = \frac{s}{t} = \frac{\Delta T\left(L_0\alpha_{\mathrm{gl}} - \alpha_{\mathrm{Si}}[n l_0 - (n-1)x_{\mathrm{O}}]\right)}{t(n-1)} \quad (1)$$

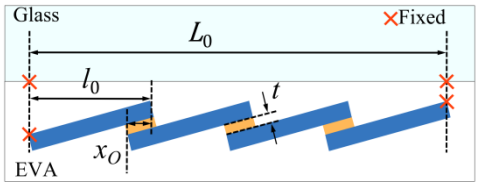

Fig. 2. Schematic drawing of model A to calculate joint shear strain forced by thermal expansion assuming that the first and last cell in a string are fixed to the glass pane [29].

γ is the shear strain which is the ratio between the relative shift s and joint thickness t. ΔT defines the temperature change, L_0 the reference glass length, l_0 the cell width and n the number of cells.

The results of a parameter study depicted in Fig. 3 estimates the shear deformations in the joint using the output parameters of Eq. 1. The results indicate on which design parameter the research for shingle cell interconnection has to focus on in order to reduce the shear stress inside the shingle joint.

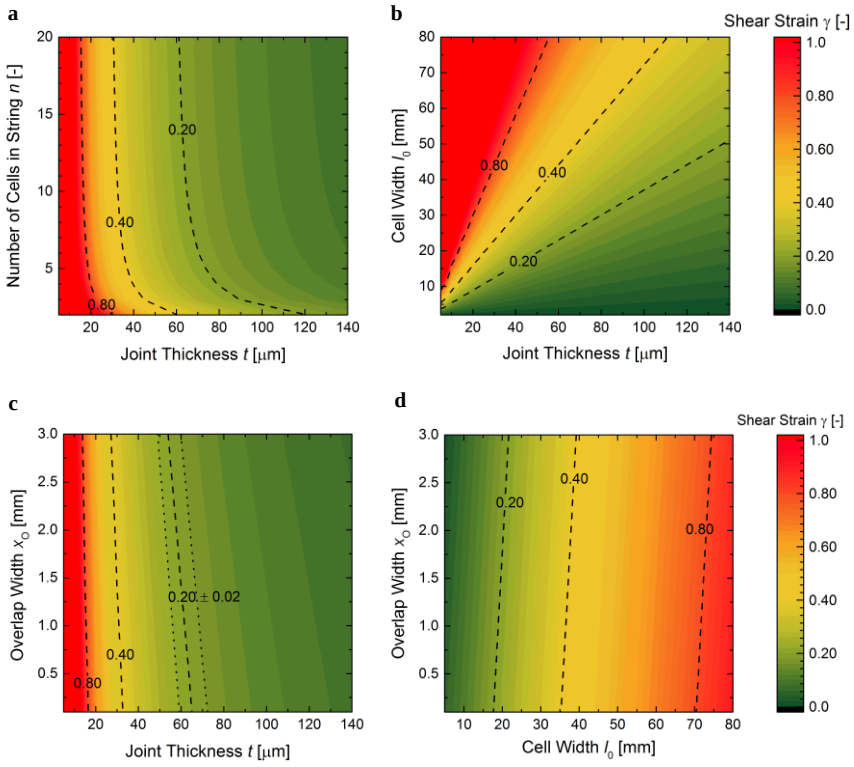

Fig. 3. Strain maps for variations of different joint parameters at $\Delta T = 125\ K$ using Eq.1. (a) shows that strain is not linked to number of cells per string for $n > 15$. (b) is calculated for $n = 30$ and depicts that cell width has a direct influence on the maximum shear strain for a given joint thickness. (c) calculated for $n = 30$ and $l_0 = 23$ mm states the strong dependence of the shear strain from joint thickness and little influence of overlap width. In (d) the influence of overlap width is also insignificant compared to varying cell widths and nearly constant for a chosen cell width assuming a representative joint thickness of $t = 50\ \mu m$.

Fig. 3a shows that when varying the number of cells strain, isolines are independent from n for $n > 15$. The shear strain is then only a function of t. Below $n = 15$ strain is not only increasing with decreasing t but also with decreasing n. This concludes that strings containing e.g. 3 - 6 cells would face higher shear stresses ($\gamma_{n=3} = 0.223$ to $\gamma_{n=6} = 0.184$) compared to strings containing up to 85 cells ($\gamma_{n=40} = 0.148$). Fig. 3b shows that both cell width and joint thickness play a significant role in shear stress of the shingle joint. Increasing cell width as well as decreasing joint thickness cause an increased shear strain. Whereas the overlap width x_O only plays a minor role compared to joint thickness and cell width (see Fig. 3c / 3d). Dotted lines in Fig. 3c illustrate the strain-isolines for a $\pm 10\%$ shift at 0.2 strain and indicate the low sensitivity of the shear strain in terms of overlap width.

2.3 Model B: thermomechanical induced strain considering a fixed bearing at the cell centers

In addition to model A published by Beaucarne [31] we propose a second approach where we assume the center of each cell to be fixed to the overlaying glass as adopted from Eitner [32]. From this assumption which is sketched in Fig. 4 we obtain model B for the estimation of thermomechanical strain according to Equation 2. With fixed cell centers the calculation is based on small repeating units and is therefore independent from the number of cells in a string. The glass reference length L_0 is expressed by the parameters l_0 and x_O. The angle between glass and solar cells is $\ll 1°$ and is therefore neglected. In one symmetry element the relative shift s of a single joint is calculated by the difference in thermal expansion between glass and silicon solar cells. As in model A any expansion of EVA, backsheet and the ECA itself are neglected in this calculation.

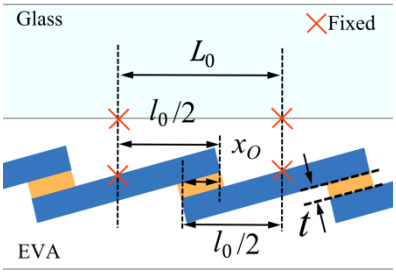

Fig. 4. Schematic drawing of the variables used to calculate joint shear strain forced by thermal expansion assuming fixed centers of solar cells (model B) [30].

$$\gamma = \frac{s}{t} = \frac{\Delta T\left(\alpha_{\mathrm{Gl}}[l_0 - x_O] - \alpha_{\mathrm{Si}} l_0\right)}{t} \qquad (2)$$

Fig. 5 shows results applying the second approach following Eq. 2 for shear strain calculation. Despite the elimination of n in model B both approaches show very similar results. This is especially valid for the influence of the remaining parameters on the strain.

We conclude that the most important parameter for reducing shear strain inside the shingle joint is the joint thickness. The cell width is limited by constraints like an efficient current transportation through fingers or the fabrication from a full sized 6“ wafer. Controlling the joint thickness is a first step towards reducing stress and strain of shingled joints and is hence expected to increase the stability of the joint in IEC 61215 TC testing. The calculated strain maps offer an effective tool to do a fast estimation of which shear strains to expect for certain geometrical parameters. For any material with a maximum shear elongation of e.g. 0.2 and cell width of 25 mm Fig. 5b shows that a joint thickness of at least 60 µm is required.

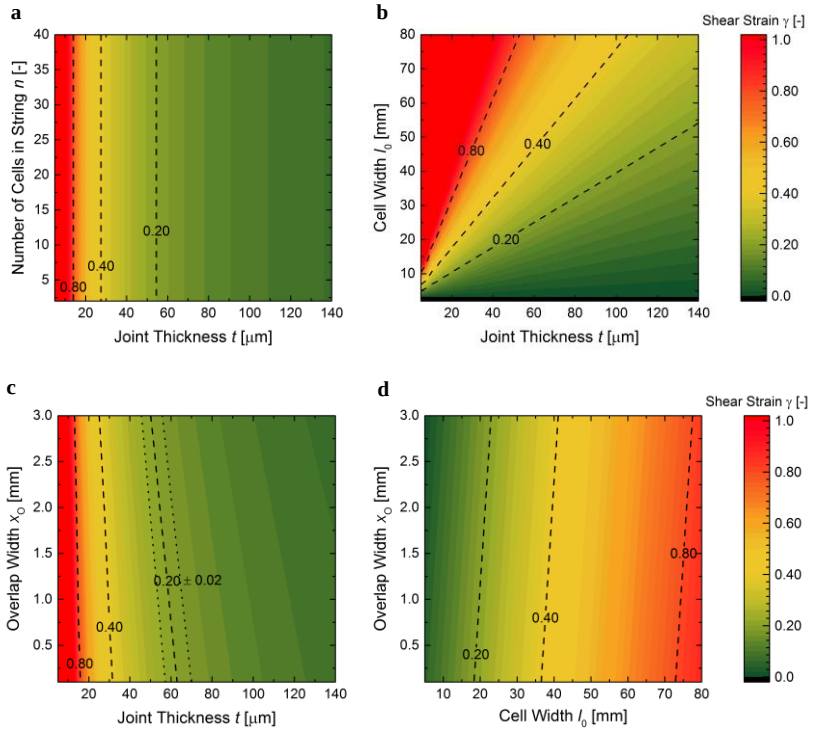

Fig. 5. Strain maps calculated for model B show the independency of strain from n (a). There are minor changes regarding the absolute values in (b), (c) and (d) compared to calculations from model A but same behavior of parameters regarding the shear strain. (c) is calculated for $l_0 = 23$ mm and (d) for $t = 50$ µm. Both state the strong dependence of strain from joint thickness and the very small influence of overlap width. Joint thickness as well as cell width strongly influence shear strain (b) whereas shear strain is quite insensitive to changes in overlap width (c) and (d).

2.4 Geometrical mismatch

Another aspect arises when shingling solar cells: geometrical mismatch. Photocurrent is proportional to the illuminated cell area. Deviations in the overlap width due to a certain machine accuracy cause a current mismatch between the cells in a string. Fig. 6 puts machine accuracy $e_{x,y,}$ in relation to the active solar cell width l_a which is the difference between cell and overlap width (l_0- x_O). For cells with $l_0 = 26$ mm, $x_0 = 2$ mm and $e_{x,y} = 0.2$ mm we calculate the deviation of the solar cell area to be 1.67 %. For even smaller cell stripes of 15 mm width - suggested to be the optimal cell size for shingling reported in [4] - the geometrical mismatch is already 2.35 %. This value adds up to the already existing electrical mismatch between solar cells and lower the string current.

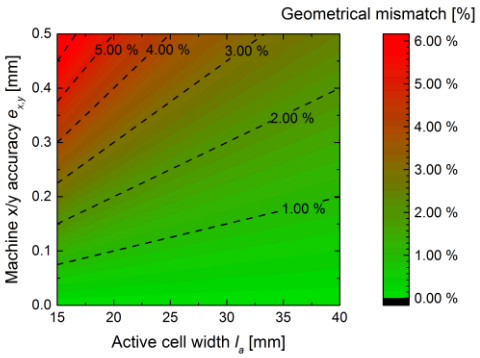

Fig. 6. Map of geometrical mismatch of the pick and place process with varying active cell widths l_a and machine accuracy $e_{x,y}$. Geometrical mismatch is corresponding to current loss in a solar cell.

3. Experimental

In the scope of this work first bifacial modules with shingled cell interconnection are built and subjected to an accelerated thermal cycling test (aTC). More detailed test parameters are given in chapter 3.2. Findings by Fujimori et al show that module testing using higher temperature changing rates than given by the IEC standard yield comparable results and failure modes [33]. This occurs in parallel to the development of special solar cells for shingling at Fraunhofer ISE [34]. There are several practical challenges to address when interconnecting bifacial solar cells. Both challenges and the processes chosen to interconnect bifacial shingle solar cells are discussed in the following.

3.1. Challenges of bifacial shingle interconnection

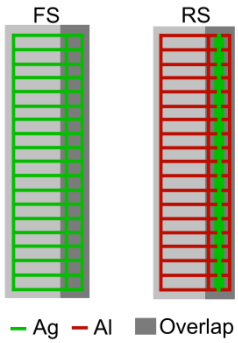

Fig. 7. Frontside (FS) and rearside (RS) metallization layout of cells used in the experiments [37].

In order to minimize module costs the overlapping area between two cells has to be as small as possible. Up to now we are applying an overlap width of typically 2 mm, however the objective is to realize overlaps well below 1 mm. The calculations of the shear strain in section 2 allow a reduced overlap width because the effect on the resulting shear strain in the shingle joint is small. In contrast to that the overlap region still has to be large enough to fit a busbar and sufficient space for a reliable interconnection. Figure 7 shows the front-side and rear-side metallization layout of the bifacial PERC cells used in our experiments. On the front side an Ag contact finger grid is applied (green) and on the rear side a Al- contact finger grind and a Ag busbar is applied in the overlap region. There is the need to cover a certain area in the overlap with ECA or solder to ensure the mechanical stability as well as sufficient electric conductivity of the joint.

Silver metallization is the standard material for front side metallization and hence well established for interconnection. Interconnecting the aluminum on the rear side of the solar cell in turn is – without special Al treatment such as proposed in [35–37] - impossible for soldering below 300 °C because of the existence of native Al_2O_3 surfaces. Typical glue as well shows poor adhesion to Al_2O_3 surfaces. A reliable interconnection hence requires interfaces preferably made of silver on both front and rear side. Therefore a combination of contacting aluminum and a non-firing through silver metallization are typically applied on the rear. An optimal overlap design features a trade-off between a minimal overlapping area and an aluminum-finger contacted silver busbar which is still completely covered by the adjacent overlapping cell.

3.2 Module fabrication and characterization

In the current study we use bifacial p-type **S**hingled **P**assivated **E**dge, **E**mitter and **R**ear (pSPEER) solar cells for module integration, which are developed at Fraunhofer ISE [34]. The SPEER cells are manufactured by laser scribing and cleaving 6” PERx-based solar cells. Passivation of the bare silicon at the edges after cleaving is currently under investigation within the cell development.

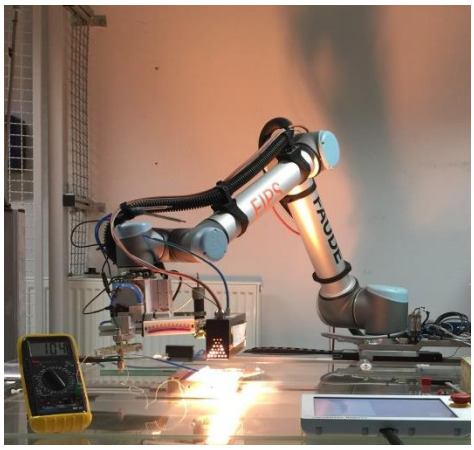

Fig. 8. *Universal Robot UR5* programmed to assemble pSPEER solar cells to shingle strings and cure ECAs with an IR radiator.

Typically three to six pSPEER cells are interconnected using either a near eutectic Sn42Bi58 solder or an epoxy-based ECA filled with 50 − 60 % silver particles. Both joint materials are manually stencil printed. The mask used for printing is 100 µm thick and features lines of 500 µm width. Within this work we investigate soldered joints as a possible alternative to the established route using ECAs. We pick and place the solar cell stripes by a Universal Robots UR5 robotic arm (Fig. 8). When manually assembling a module with very high accuracy a metal step device as shown in Fig. 9 is used. Its placement accuracy is equal to the fabrication machine accuracy ($e_{x,y} = 0.02$ mm). After applying solder paste, the cells are arranged one by one and fixed on the steps by applying vacuum. Low temperature solder paste is liquefied during lamination at 160 °C because of its melting point of 139 °C. The module stack is completed by a 3 mm white glass, standard EVA and transparent ETFE backsheet.

Fig. 9. Step device for high accuracy ($e_{x,y} = 0.02\ mm$) arranging of pSPEER solar cells to strings.

Laminated modules are characterized using an electroluminescence and an I-V measurement system. Both front and rear side EL images and I-V characteristics are then compared before and after temperature cycling in order to investigate joint stability. A temperature chamber with a maximum rate of 8 K/min is employed for an accelerated TC200 (aTC) testing. The aTC testing deviates from IEC 61215 TC200 testing by applying maximum heating and cooling rates of 8 K/min and 15 min dwell times at −45 °C and 85 °C. Furthermore we investigate the joint using X-ray transmission imaging, SEM imaging and energy dispersive X-ray spectroscopy.

4. Results and Discussion

Table 2 shows the I-V-characteristics of the shingle module containing three cells interconnected with Sn42Bi58 solder paste. The absolute power degradation after aTC200 is 4.2 %. The results reveal a successful integration of pSPEER solar cells to modules reaching an initial fill factor of 77 % and an efficiency of 18.2 %. The drop in the fill factor after aTC200 is supposedly caused by degradation of the solder interconnection and therefore a higher series resistance in the joint. This leads to a loss in efficiency of 0.8 % absolute but still above the IEC 61215 criterion of less than 5 % power loss.

Table 2. I-V data of a three cell shingle module before and after aTC200 with SnBi low temperature solder joints

aTC	I_{SC} (A)	V_{OC} (V)	FF (%)	η (%)	P_{MPP} (W)	$P_{MPP,rel.}$ (%)
0	1.175	1.934	77.0	18.2	1.750	100
200	1.177	1.922	74.1	17.4	1.677	95.8

EL images of the shingle module show initially homogeneous current distributions as shown in Fig. 10. The interconnection slightly degrades after aTC 200. Starting at aTC 75 EL images show brighter areas around the rear side contact pads of the silver busbar. These areas further increase until 200 cycles indicating a decline in joint conductivity next to the contact pads. Additionally a crack appears after aTC75, which follows the rear side busbar of the right cell. We link this to the interface of co-fired Ag/Al metallization as described by Schmidt [38]. The combination of both metals cause residual stresses in the silicon bulk which lower the value for external stresses to cause cracks in the silicon. If occurring more frequently in further experiments this needs to be addressed e.g. by reducing the amount of contact points between fingers and busbar.

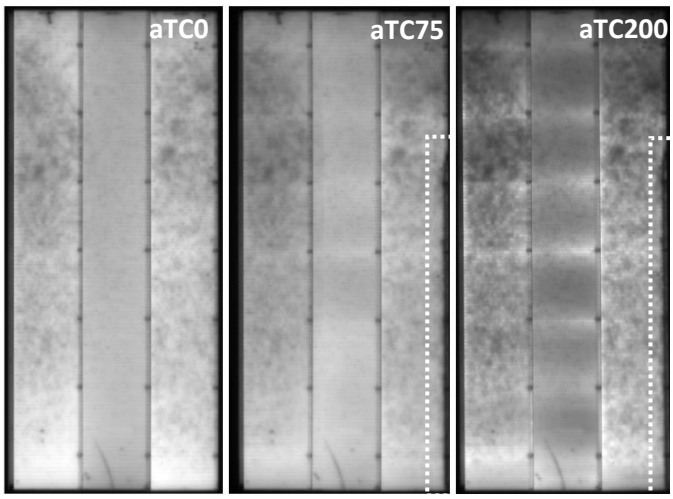

Fig. 10. EL images of a three cell shingle module at different aTC-stages (aTC0, aTC75, aTC200) featuring a Sn42Bi58 low temperature solder interconnection. The area separated by dotted lines indicates a crack following the rear side metallization.

As shown in X-ray transmission imaging (Fig. 11a), the solder, which is initially printed in straight lines on the solar cell, shows periodic structures in the overlap after the soldering process. Both the front and the rear side silver busbar are also printed in straight lines. However the rear side busbar is partially overlapped by aluminum fingers. SEM top view images of a rear side busbar in Fig. 11b show Al contact fingers (1) and the Ag busbar (2). Additionally a circular third phase (3) around the fingers is visible. Performing EDX measurements, we find this area either to be covered by Al or consisting of an Ag/Al phase [39] (Fig. 11b). The EDX element mapping indicates a good correspondence between phase (3) and structures found in the Al mapping (4). In those areas (3), the SnBi solder does not wet the surface which explains the resulting shapes visible in the X-ray images. Good wettability is only reached on the non-influenced area of the Ag busbar (5), which significantly reduces the contact area needed for a reliable solder joint. Based on these results we assume this to be the reason for the observed FF degradation in an aTC test. The thin solder bridges between the solder dots are likely to fail first and subsequently damage also the remaining interconnection.

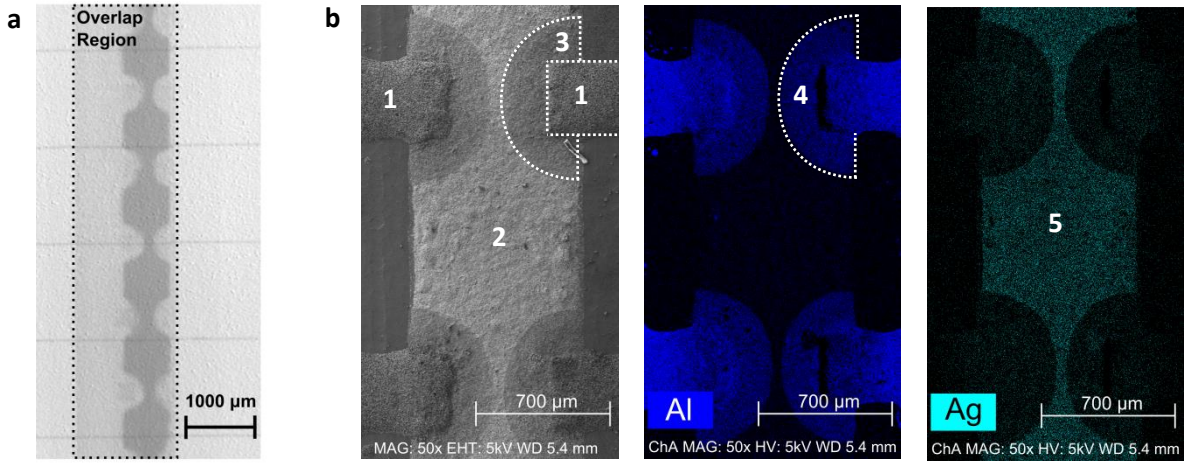

Fig. 11. X-ray transmission images of the overlap region (dotted box) (a) and top view SEM images with EDX mapping of the rear side busbar (b). The Al fingers (1) touch the Ag busbar (2) and an Al/Ag phase (3) forms reducing the available Ag surface for interconnection. Solder is dewetting from Al containing surfaces (4) only establishing a connection where sufficient silver is present (5).

5. Conclusion

This work reviews the history and scientific state of the art of shingling interconnection technology. Starting from the 1960's publications show, that shingling is potentially applicable throughout a wide range of solar cell technologies like front to back c-Si / mc-Si, thin-film a-Si or CIGS. However until today shingling has been a technique for high efficient niche applications and therefore not subject to extensive research. With first industrial products available on the market more profound scientific investigations are needed to prove advantages and reliability of this module topology.

We address one of the crucial aspects for a success of the shingle concept: thermomechanical reliability of the joint. We discuss two approaches to estimate shear strain of the joint caused by thermal expansion and contraction of the module. Considering standard values for $1/6^{th}$ cells with 25 mm cell width and an overlap width of 2 mm the strain varies between 0.055 and 1.090 for joint thicknesses of 200 µm and 10 µm respectively. For a joint thickness of 50 µm, the strain resulting from a temperature change of 125 K varies between 0.200 and 0.244 for overlap widths between 3.0 mm and 0.5 mm respectively. In order to reduce shear strain for shingle interconnection, we conclude that the most relevant parameter is the joint thickness, whereas overlap width and number of cells play a minor role.

We further present first results for module integration of bifacial pSPEER solar cells especially developed for shingling. We use low temperature SnBi solder to fabricate 3-cell-modules in a combined soldering and lamination

process. The module shows a power loss of $< 5\,\%$ after 200 accelerated TC cycles and hereby meets the IEC 61215 criterion. Even though calculations indicate the same or less strain with increasing string length, the reliability of longer strings in thermocycling still has to be proven in further experiments. We attribute the observed FF loss of about 3 % absolute to an inhomogeneous solder distribution in the overlap area. This originates from either an Al layer or an Ag/Al phase formed at the rear side metallization at the overlap of contact fingers and busbar. SnBi solder dewets from these areas, hence this significantly reduces the contact area for interconnecting the solar cells.

Acknowledgements

The authors thank Puzant Baliozan, Elmar Lohmüller and Tobias Fellmeth from Fraunhofer ISE for providing pSPEER cells for module integration. Measurements of I-V-curves where under the responsibility of Felix Martin and have been a great source of information. This work has been supported by the Federal Ministry of Economic Affairs and Energy (BMWi) under the contract number 0324125, acronym PV-BAT400.

References

[1] D. C. [J.] Dickson, “Photovoltaic semiconductor apparartus or the like,” US 2938938 A, May 31, 1960.
[2] M. Müller, G. Fischer, B. Bitnar, S. Steckemetz, R. Schiepe, M. Mühlbauer, R. Köhler, P. Richter, C. Kusterer, A. Oehlke, E. Schneiderlöchner, H. Sträter, F. Wolny, M. Wagner, P. Palinginis, and D. H. Neuhaus, “Loss analysis of 22% efficient industrial PERC solar cells,” Energy Procedia, vol. 124, pp. 131–137, 2017.
[3] U. Eitner, M. Köntges, and R. Brendel, “Measuring Termomechanical Displacement of Solar Cells in Laminates Using Digital Image Correlation,” IEEE, 2009.
[4] Nico Wöhrle, Aina Alapont Sabater, and Johannes Greulich, “Genuine Bifacial Simulation and Optimization of an mc-Silicon PERC Solar Cell,” in Proceedings of the 33rd European Photovoltaic Solar Energy Conference and Exhibition, 2017.
[5] N. Woehrle, Lohmüller E., M. Mittag, A. Moldovan, Baliozian P., T. Fellmeth, Krauss K., A. Kraft, and R. Preu, “Solar cell demand for bifacial and singulated-cell module architectures,” 36th Photovoltaics International, pp. 48–62, 2017.
[6] M. Mittag, T. Zech, M. Wiese, D. Blaesi, M. Ebert, and H. Wirth, “Cell-to-Module (CTM) analysis for photovoltaic modules with shingled solar cells,” in 44th IEEE PV Specialist Conference PVSC.
[7] D. M. Chapin, C. S. Fuller, and G. L. Pearson, “A new silicon P-N junction photocell for converting solar radiation into electrical power,” J Appl Phys, vol. 25, no. 5, pp. 676–677, 1954.
[8] R.J. Nielsen and L. Rongved, “Sattelite Solar Cell Assembly,” US3116171, Dec 31, 1963.
[9] W.R. Cherry, “Status of Photovoltaic Solar Energy Converters,” IEEE Transactions on Aerospace and Electronic Systems, vol. 1, no. 1, 1965.
[10] R. S. Scharlack, EFG Solar Modules: Final Report. (No. DOE/JPL/954999-1), 1978.
[11] D. A. Dilts and T. W. Brauneck, “Flexible, interconnected array of amorphous semiconductor photovoltaic cells,” US 4617420, Oct 14, 1986.
[12] D. Snowdon, J. Green, Cousins P., S. Stone, R. Simpson, and J. E. Cotter, “Composite Curved Laminates for the UNSW Sunswift II Solar Array,” in ISES Solar World Congress 2001, pp. xi–xiii.
[13] M. A. Green, “The 1996 World Solar Challenge Solar Car Race Across Australia,” Prog. Photovoltaics Res. Appl. (Progress in Photovoltaics: Research and Applications), no. 5, pp. 69–76, 1997.
[14] W. Schmidt and K.-D. Rasch, “New interconnection technology for enhanced module efficiency,” IEEE Trans. Electron Devices, vol. 37, no. 2, pp. 355–357, 1990.
[15] J. Zhao, A. Wang, E. Abbaspour-Sani, F. Yun, and M. A. Green, “Improved efficiency silicon solar cell module,” IEEE Electron Device Lett., vol. 18, no. 2, pp. 48–50, 1997.
[16] S. W. Glunz, J. Dicker, M. Esterle, M. Hermle, J. Isenberg, F. J. Kamerewerd, J. Knobloch, D. Kray, A. Leimenstoll, F. Lutz, D. Osswald, R. Preu, S. Rein, E. Schaffer, C. Schetter, H. Schmidhuber, H. Schmidt, M. Steuder, C. Vorgrimler, and G. Willeke, “High-efficiency silicon solar cells for low-illumination applications,” in Conference Record of the Twenty-Ninth IEEE Photovoltaic Specialists Conference 2002, May. 2002, pp. 450–453.

[17] L. Fraas, R. Ballantyne, S. Hui, S.-Z. Ye, S. Gregory, J. Keyes, J. Avery, D. Lamson, and B. Daniels, "Commercial GaSb cell and circuit development for the Midnight Sun[sup ®] TPV stove," in : AIP, 1999, pp. 480–487.
[18] R. G. Mahorter, B. Wernsmann, R. M. Tomas, and R. R. Siergiej, "Thermophotovoltaic system testing," Semicond. Sci. Technol., vol. 18, no. 5, pp. 232–240, 2003.
[19] M. Pinarbasi and B. Metin, "Methods of interconnecting thin film solar cells," US 2012/0318319 A1, Dec 20, 2012.
[20] A. Neisser, C. A. Kaufmann, R. Klenk, R. Scheer, M. A. Kroon, G. Oomen, and H.-W. Schock, "Prototype development - flexible Cu(In,Ga)Se2 thin film solar cells for space applications," in Conference Record of the Thirty-first IEEE Photovoltaic Specialists Conference, 2005, pp. 227–230.
[21] P. Reinhard, S. Buecheler, and A. N. Tiwari, "Technological status of Cu(In,Ga)(Se,S)2-based photovoltaics," Solar Energy Materials and Solar Cells, vol. 119, pp. 287–290, 2013.
[22] C. Tzikas, G. Gómez, M. van den Donker, K. Bakker, A. H.M. Smets, and W. Folkerts, "Do Thin Film PV Modules Offer an Advantage under Partial Shading Conditions," in Proceedings of the 33rd European Photovoltaic Solar Energy Conference and Exhibition, 2017.
[23] L. Mattos, "Final Technical Progress Report: High-Efficiency Low-Cost Thin-Film GaAs Photovoltaic Module Development Program," no. No. NREL/SR-5200-54398, National Renewable Energy Laboratory (NREL), 2012.
[24] F. Stefani, "Process for connecting photovoltaic cells in series, a photovoltaic cell connectable in series using the process, and a module obtained with the process," US 2010/0218799 A1, Sep 2, 2010.
[25] R. P. Stoehr, P. Simpson, and A. Shibata, "System and method for dentritic web solar cell shingling," US 2003/0121228 A1, Jul 3, 2003.
[26] R. Morad, G. Almogy, I. Suez, J. Hummel, N. Beckett, Y. Lin, D. Maydan, and J. Gannon, "Shingled solar cell module," US 9484484 B2.
[27] M. Pinarbasi, E. Lee, S. Erdemli, and E. Petrushansky, "Methods for interconnecting photovoltaic cells," US2012/0125391A1, May 24, 2012.
[28] Sung Edward and J. Zu-Yi Liu, "Systems, Method and Apparatus for curing conductive paste," US9748434B1, USA, Aug 29, 2017.
[29] R. Snow, E. Lee, M. Burak, E. Serkan, and A. Anjuli, "Solar cell with grid wire interconnections," US2012/0325282A1, Dec 27, 2012.
[30] H. Flödl, "Solar Cell Module," US 4877460, Oct 31, 1989.
[31] G. Beaucarne, "Materials Challenge for Shingled Cells Interconnection," Energy Procedia, vol. 98, pp. 115–124, 2016.
[32] U. Eitner, M. Koentges, and R. Brendel, "Use of digital image correlation technique to determine thermomechanical deformations in photovoltaic laminates: measurements and accuracy," Sol Energ Mat Sol C, vol. 94, no. 8, pp. 1346–1351, 2010.
[33] M. Fujimori, T. Kohno, Y. Tsuno, and K. Morita, "Applicability of Highly Accelerated Thermal Cycling Testing for Multiple Types of Polycrystalline Silicon Photovoltaic Modules," in Proceedings of the 33rd European Photovoltaic Solar Energy Conference and Exhibition, 2017, pp. 1694–1697.
[34] P. Baliozian, E. Lohmüller, T. Fellmeth, N. Wöhrle, A. Krieg, and R. Preu, "Bifacial p-type silicon shingle solar cells - the pSPEER concept," Sol. RRL, vol. 1700171, 2018.
[35] H. Nagel, M. Kamp, D. Eberlein, A. Kraft, J. Bartsch, M. Glatthaar, and S. W. Glunz, "Enabling Solderability of PVD Al Rear Contacts on High-Efficiency Crystalline Silicon Solar Cells by Wet Chemical Treatment," in Proceedings of the 32nd European Photovoltaic Solar Energy Conference and Exhibition, 2016, pp. 48–52.
[36] H. von Campe, S. Huber, S. Meyer, S. REIFF, and J. Vietor, "Direct tin-coating of the aluminum rear contact by ultrasonic soldering," in Proceedings of the 27th European Photovoltaic Solar Energy Conference and Exhibition, 2012, pp. 1150–1153.
[37] P. Schmitt, D. Eberlein, C. Ebert, M. Tranitz, U. Eitner, and H. Wirth, "Adhesion of Al-metallization in ultra-sonic soldering on the Al-rear side of solar cells," Energy Procedia, vol. 38, no. 0, pp. 380–386, 2013.

[38] C. V. Schmid, “Schadensmechanismen bei Silizium-Solarzellen und Maßnahmen zur Festigkeitserhöhung,” Materialwissenschaft und Werkstofftechnik, Maschinenbau, Karlsruher Institut für Technologie, Karlsruhe, 2010.
[39] H. Baker, Alloy Phase Diagrams: ASM Handbook, 3rd ed.: ASM International, 2016.